

# Advances in Ultrasonic Imaging for Internal Flaws in Structures

Thompson Vu Nguyen<sup>1</sup>, Simone Sternini<sup>2</sup>, and Francesco Lanza di Scalea<sup>3</sup>

<sup>1,2</sup> *PhD Candidate, Department of Structural Engineering, La Jolla, California, 92093, USA*

*tvn007@eng.ucsd.edu*

*ssternin@eng.ucsd.edu*

<sup>3</sup> *Professor, Department of Structural Engineering, La Jolla, California, 92093, USA*

*flanzadiscalea@ucsd.edu*

## ABSTRACT

In the field of non-destructive testing of structures, 3D imaging of internal flaws is a critical task. Defect imaging allows the engineer to make informed follow-up decisions based on the morphology of the flaw.

This paper will present advances in ultrasonic tomography for the 3D visualization of internal flaws in solids. In particular, improvements to the conventional tomographic imaging algorithms have been made by utilizing a mode-selective image reconstruction scheme that exploits the specific displacement field, respectively, of the longitudinal wave modes and the shear wave modes, both propagating simultaneously in the test volume. The specific mode structure is exploited by an adaptive weight assignment to the ultrasonic tomographic array. Such adaptive weighting forces the imaging array to look at a specific scan direction and better focus the imaging onto the actual flaw (ultrasound reflector).

This study shows that the adaptive weighing based on mode structure improves image contrast and resolution compared to a conventional ultrasonic imaging technique based on delay-and-sum. Results will be shown from simulations and imaging experiments of simulated flaws in an aluminum block.

## 1. INTRODUCTION

Non-invasive 3D imaging techniques are essential to providing a comprehensive diagnosis and prognosis of potentially damaged structures and materials. Ultrasonic and thermal waves can be used in such non-destructive evaluation (NDE) techniques in a variety of applications such as structural health monitoring (SHM), material characterization, flaw detection and characterization, etc. As such, applications of ul-

trasonic arrays have widely been used in the NDE / SHM field and the medical diagnostic imaging field.

In the literature, advances in the ultrasonic imaging field has been made possible by synthetic apertures and beamforming frameworks. In one application, by manipulation of transmission sequences from the transducer elements, the array can transmit a global wave front such as plane waves (Garcia et al., 2013),(Ekroll et al., 2013),(Salles et al., 2014) and circularly-crested waves from virtual sources (Frazier & O'Brien, 1998),(Nikolov & Jensen, 2000). These advances provides a greater advantage by minimizing the transmissions while producing more energy in the wavefront. In reception, the full matrix capture (FMC) waveforms are collected and processed through various beamforming algorithms. There are several frameworks in the ultrasound imaging community that have been explored.

Both the conventional and proposed beamforming algorithms utilize a FMC in the processing. Conventional delay-and-sum (DAS) algorithms are typically used for fast and robust image reconstruction. DAS combines the summation of the responses from all the elements for a given pixel point by applying calculated delays, or time-of-flight (TOF), across the elements in the array. A different approach using the minimum-variance distortionless algorithm (MVD), also known as the Capon method, has been used in various array processing applications. This method improves the quality and accuracy of the images by applying different weights in addition to the summation of the waveforms to the DAS algorithm to minimize noise, thereby, improving the clarity of the image. (Hall & Michaels, 2010),(Austeng et al., 2011).

In this paper, a new adaptive beamforming framework is presented. A set of global matched coefficient weights (GMC) is introduced to be used in conjunction with the mentioned beamforming frameworks. By exploiting the correlation of the expected response and the recorded response from the elements in the array, this additional information can improve

---

Thompson Vu Nguyen et al. This is an open-access article distributed under the terms of the Creative Commons Attribution 3.0 United States License, which permits unrestricted use, distribution, and reproduction in any medium, provided the original author and source are credited.

the overall quality and accuracy of the image. The GMC can be applied to existing algorithms such as the DAS and MVD. Because these GMC rely on an expected response, specific replica vectors are introduced. By extracting the out-of-plane component from the surface of the transducer, the replica vectors are here calculated using two modes of propagation, specifically the longitudinal wavemode transmission to longitudinal wavemode reception (L-L) and the shear wavemode transmission to longitudinal wavemode reception (L-S). Other combinations of wavemodes can also be exploited, but in this paper, only the two mentioned will be discussed.

The paper is structured in the follow portions: (1) modes of transmissions, (2) adaptive beamforming techniques (3) correlation coefficient weights, (4) simulation and experimental configurations, and (5) results and conclusions.

## 2. MODES OF TRANSMISSIONS

There are several conventional ways to excite the elements of an array. First, in the synthetic aperture approach, a sequence encompassing all elements, or a selected number of sparse elements can input a pulse, one element at a time, into the test specimen (Lockwood et al., 1998). The objective is to illuminate the scatterers from multiple directions. This produces a better resolution image. This is a very common method of transmission.

In another mode, multiple transducer elements can be fired simultaneously to produce a plane wave, or the elements can have a linear time-delay applied across the elements to produce an inclined plane wave (Garcia et al., 2013),(Ekroll et al., 2013),(Salles et al., 2014). This aim of this method is to transfer the maximum amount of energy from multiple angles in minimum numbers of transmissions as compared to the first method.

The third method is to use a virtual source. Usually a virtual element is placed behind the array. The distance between the elements of the array and the virtual element can be used to calculate the delayed time in transmission. This set of time delays are applied to the elements in the array (Frazier & O'Brien, 1998), (Nikolov & Jensen, 2000). This virtual source method allows more energy in the immediate wavefront with fewer transmissions as compared to the first method. Similar to the first method, by using several virtual sources, scatterers can be illuminated from various angles enhancing the clarity of the image.

## 3. BEAMFORMING TECHNIQUES

With these several methods of excitations, the data collected in reception from the elements in the array can be processed in several ways. The different algorithms have one common fundamental: synthetic aperture beamforming. By shift-

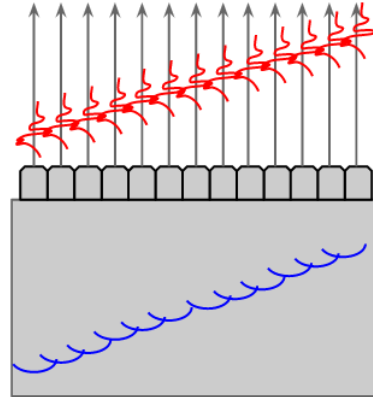


Figure 1. An example of a plane wave excitation. Incremental trigger delays were applied to the transducers, resulting in an offset linear wavefront.

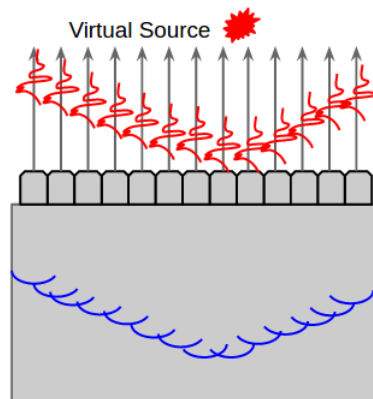


Figure 2. An example of a virtual source excitation. Calculated trigger delays for each transducer were applied, with respect to the distance of the virtual source. This resulted in a larger wavefront amplitude.

ing the waveform in different time-delays, the scatterer location or pixel location can synthetically be focused. This section will review two conventional algorithms: the delay-and-sum (DAS) and the minimum variance distortionless method (MVD). Following, two additional algorithms are presented with the proposed adaptive weights. In all waveforms used to process, the differential signals of the baseline signals and test signals are used. Baseline signals are defined as signals collected from a non-defect specimen, and the test signals are from the unknown specimen.

$$A_{ij} = A_{ij}^{test} - A_{ij}^{base} \quad (1)$$

### 3.1. Delay-and-Sum

The conventional delay-and-sum (DAS) shifts and sums the waveforms from each element in accordance to the desired scatterer. The total distance of the wavepath from the transmitter to the scatterer location and the return path from the scatterer location to a receiver is calculated. Using the proper velocity, a TOF can be found. This is processed for each receiver for each transmitter. More explicitly, for transmitter  $i$ -th transmitter and  $j$ -th receiver, with a scatterer located at  $(x,y)$ , the delay time is calculated as:

$$\tau_{ij,xy} = \frac{d_{ij,xy}}{v} \quad (2)$$

where

$d_{ij,xy}$  is the distance of the wave propagation from the  $i$ -th transmitter to the scatterer at  $(x,y)$  to the  $j$ -th receiver

$v$  is the medium velocity

Translated into pixel values, for  $N$  transmissions and  $M$  receivers, the intensity is defined as:

$$P_{xy} = \left| \sum_i^N \sum_j^M w_{ij,xy} A_{ij}(\tau_{ij,xy}) \right|^2 \quad (3)$$

where

$w_{ij,xy}$  is the unique weighting coefficient for the  $i$ -th transmission, the  $j$ -th receiver, and the pixel  $(x,y)$

$A_{ij}$  is the amplitude value of the waveform for the  $i$ -th transmission to the  $j$ -th receiver at the delayed time  $\tau_{ij,xy}$

In matrix form, it can be expressed as:

$$P_{xy} = w_{xy}^T R_{xy} w_{xy} \quad (4)$$

where

$w_{xy}$  is the vector of weighting coefficients,  $w_{ij,xy}$  for the pixel  $(x,y)$

$T$  denotes the Hermitian transpose

$R_{xy}$  is the auto-correlation matrix:  $r_{xy} r_{xy}^T$

$r_{xy}$  is the vector of all  $A_{ij}(\tau_{ij,xy})$  values for the pixel  $(x,y)$

For the conventional DAS imaging algorithm, the weighting coefficients,  $w_{ij,xy}$  are uniform. However, a window function can be used here to minimize sidelobes. For this paper, the weighting coefficients will be uniform (i.e., equal to 1), and thus will be neglected.

### 3.2. Minimum Variance Distortionless Method

Although DAS will produce fair quality images, the minimum variance distortionless method can potentially produce more accurate and lower noise images by applying adaptive weights for  $w_{xy}$  in equation (4). By minimizing unwanted scattering reflections, the clarity of the image increases. This framework is formed by using a replica vector,  $e_{xy}$ , and by satisfying the two conditions (Kuperman & Turek, 1997):

$$P_{xy} = \min_w w_{xy}^T R_{xy} w_{xy} \quad (5)$$

$$w_{xy}^T e_{xy} = 1 \quad (6)$$

By using Lagrange multipliers,  $w_{xy}$  can be expressed as:

$$w_{xy}^{MV} = \frac{R_{xy}^{-1} e_{xy}}{e_{xy}^H R_{xy}^{-1} e_{xy}} \quad (7)$$

where  $-1$  denotes the inverse. The final MVD form is:

$$P_{xy} = (w_{xy}^{MV})^T R_{xy} (w_{xy}^{MV}) \quad (8)$$

or, by substitution:

$$P_{xy} = \frac{1}{(e_{xy})^T R_{xy}^{-1} (e_{xy})} \quad (9)$$

In summation form:

$$P_{ij,xy} = \left| \sum_i^M \sum_j^N w_{ij,xy}^{MV} A_{ij}(\tau_{ij,xy}) \right|^2 \quad (10)$$

#### 3.2.1. Replica Vectors

In most applications of the MVD method, replica vectors are features typically extracted from analytical or numerical modelling for the specific scatterer location. For example, some replica vectors are derived from the calculated expected time of arrival for various scattering sources coupled with the expected attenuation in a medium (Chen et al., 2014). In ocean acoustics and geophysics, the vectors are extracted from the expected frequency spectrum across the the array from the numerical simulated waveforms for each noise source (Baggeroer et al., 1993) (Corciulo et al., 2012). In structural vibrations, the vector of expected deflections for the nodes of a rigid bar for all possible loading locations are

the replica vectors (Kuperman & Turek, 1997). Essentially, across the domains of utilizing replica vectors in the MVD or Capon's method, a modeled expected response is used.

In the application of ultrasound imaging, the replica vectors can be described as the expected signals of the array, from all scattering sources in the imaging domain. In this paper, the replica vectors will be utilizing the expected amplitudes of the longitudinal wavemodes. More specifically, the out-of-plane component of the received waves are considered, to model the expected response from longitudinal transducers. For simplification, a 2D medium model was used to extract these amplitudes.

Although only one wavemode is of interest, two combinations of the overall wavemodes are considered to use with the replica vectors. First, the longitudinal wavemode in transmission coupled with the longitudinal wave mode in reception ( $L-L$ ). Second is the shear wavemode in transmission with the longitudinal wavemode in reception ( $L-S$ ). Essentially, the perpendicular component to the surface was extracted from the location of the sensors to best model the expected response of a longitudinal type transducer as shown in Figure 3. The return path to the sensors are the same for both cases, the replica vectors,  $e_{ij,xy}$ , are the same for both combinations. Therefore, the replica vectors,  $e_{ij,xy}$ , depend on the wavemode arrivals in  $A_{ij}(\tau_{ij,xy})$ , and the locations of the transducer receiver with respect to the scatterer. These are derived from trigonometric considerations of the particle displacement field specific to the wavemodes as shown:

$$e_{ij,xy}^{(L-L),(S-L)} = \left| \frac{y - y_j}{\sqrt{((x - x_j)^2 + (y - y_j)^2)}} \right| \quad (11)$$

For completion, using trigonometric relationships of the displacement field of a shear reflection response, the shear wave-mode combinations from the scatterer to the transducer receivers are calculated as:

$$e_{ij,xy}^{(S-S),(L-S)} = \left| \frac{x - x_j}{\sqrt{((x - x_j)^2 + (y - y_j)^2)}} \right| \quad (12)$$

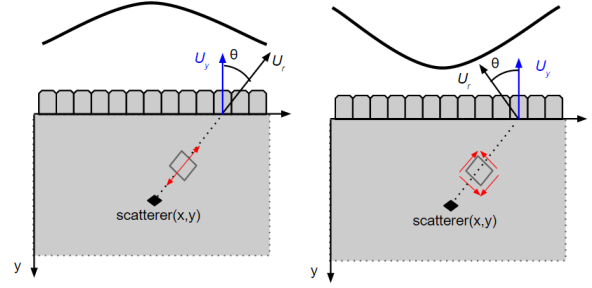


Figure 3. Depiction of transmitter receiver pair  $i - k$  for the  $i^{th}$  transmitter. The  $y - th$  or perpendicular component of the reflection due to the scatterer  $(x, y)$  is only considered to accurately represent the out-of-plane pressure component that a longitudinal transducer would receive. Top: due to a longitudinal wave mode reflection. Bottom: due to a shear wave mode reflection.

#### 4. GLOBAL MATCHED COEFFICIENTS (GMC)

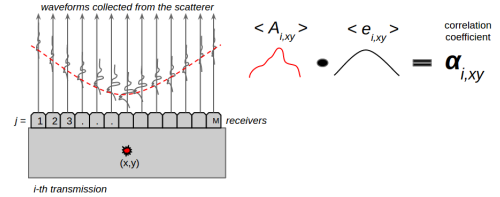


Figure 4. Correlation coefficient depiction for a response to an  $i - th$  transmission and a scatterer at  $(x, y)$ . The observed amplitudes extracted at  $\tau_{ij,xy}$  is  $A(\tau_{ij,xy})$  and the expected amplitudes or the replica vector is denoted as  $e_{i,xy}$  for a longitudinal reflection mode as defined in equation (11).

In addition to these beamforming algorithms, there is another level of weights to explore. Given that the expected values are known for each transmission - receivers combinations for all scatterer locations, a correlation factor,  $\alpha_{i,xy}$  can be calculated to determine the significance of the data received in a more global perspective. For the conventional DAS algorithm, the weight is applied as:

$$P_{ij,xy} = \left| \sum_i^N \sum_j^M \alpha_{ij,xy} A_{ij}(\tau_{ij,xy}) \right|^2 \quad (13)$$

where  $\alpha_{ij,xy}$  is the cross-correlation at zero-lag, or the inner product, of the expected values vector and the observed values super-vector for all transmissions.

$$\alpha_{ij,xy} = \sum_i^N \sum_j^M e_{ij,xy} A_{ij}(\tau_{ij,xy}) \quad (14)$$

After substitution, this can be expressed as:

$$P_{ij,xy} = \left| \sum_i^N \sum_j^M e_{ij,xy} A_{ij}(\tau_{ij,xy}) \right|^2 \quad (15)$$

or in matrix form:

$$P_{xy} = \alpha_{xy}^2 w_{xy}^T R_{xy} w_{xy} \quad (16)$$

For the MVD framework considering the  $\alpha_{i,xy}$  terms, the image operator can be expressed as:

$$P_{ij,xy} = \left| \sum_i^N \sum_j^M w_{ij,xy}^{MV} A_{ij}(\tau_{ij,xy}) \right|^2 \quad (17)$$

and in matrix form:

$$P_{xy} = \alpha_{xy}^2 (w_{xy}^{MV})^T R_{xy} (w_{xy}^{MV}) \quad (18)$$

setting  $w_{xy}^{MV}$  as in equation (7) gives:

$$P_{xy} = \frac{\alpha_{xy}^2}{(e_{xy})^T R_{xy}^{-1} (e_{xy})} \quad (19)$$

## 5. SIMULATIONS

To determine how these different methods compare using the GMC, an aluminum block with several defects (top drilled holes) was the test subject. Numerical simulations were conducted to extract waveforms and experiments were carried out. The waveforms were compared to verify the simulation results. Imaging algorithms were then applied to both simulation waveforms and experimental waveforms.

### 5.1. Numerical simulation

Numerical simulations were carried out using k-Wave, an open source MATLAB toolbox used to model elastic waves (MATLAB, 2010) (Treeby et al., 2014). From the simulation, a FMC data structure can be captured. The FMC provided sets of waveform data to be processed in the prior discussed conventional beamforming frameworks with and without the global matched coefficients.

Several numerical models were conducted. First, numerical models were conducted with a defected aluminum block. Typical synthetic aperture excitations produced waveforms to be used in conventional beamforming frameworks and global adaptive beamforming frameworks. These results will be validated with experimental results, presented in the next section. Numerical simulations with a defective rail were also conducted.

### 5.2. Simulation configuration

The simulation considered a aluminum block modeled in 2D with a defect (hole) towards the center of the plate (Figure 5). Impulse excitations centered at 2.25 MHz were generated with linear array. A 32-element linear array was simulated at the side of the block. The arrays followed a synthetic focusing aperture scheme, exciting element by element with a FMC. The TOF can be extracted using trigonometry relationships.

Simulations also included cases when the aluminum block had no defects to serve as a baseline.

Table 1. Simulated aluminum block

density	2710 kg/m <sup>3</sup>
$v_L$	6150 m/s
$v_S$	3050 m/s
width	57.7 mm
length	57.7 mm
height	57.7 mm

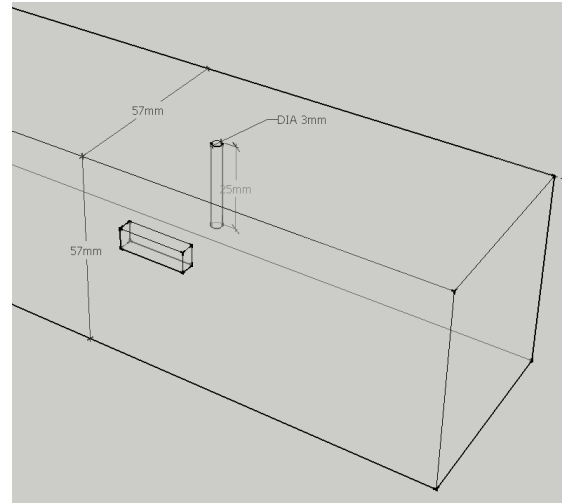


Figure 5. Configuration of linear array on the side of the aluminum block with a defect (cylindrical void).

### 5.3. Experimental configuration

The experiment involves an aluminum block with identical cross section dimensions as in table 1. However, only a portion of the block is used to minimize boundary reflections. The block with the defect is shown below. The excitation mode is identical to the simulation, with an element-by-element excitation, each with a FMC.

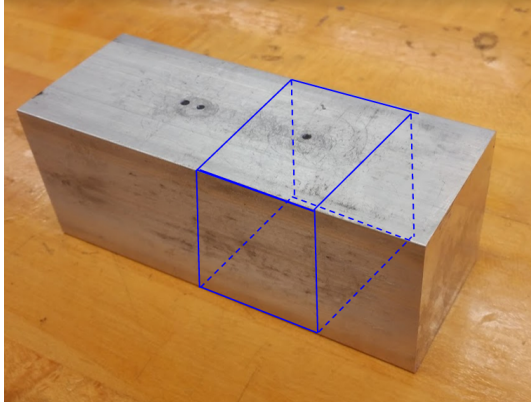


Figure 6. Image of defective block with a top drilled hole considered in experiment.

The array used has the properties below in table 2. The acquisition system is made by Advanced OEM Systems (*Advanced OEM Systems*, n.d.). This digitizer is a FPGA system that is a fully data acquisition system. Data is extracted and loaded into MATLAB for analysis.

Table 2. Linear array

elements	32
$f_0$	2.11 MHz
frequency band	0.1 MHz
pitch ( $p$ )	0.6 mm
connector	Omniscan

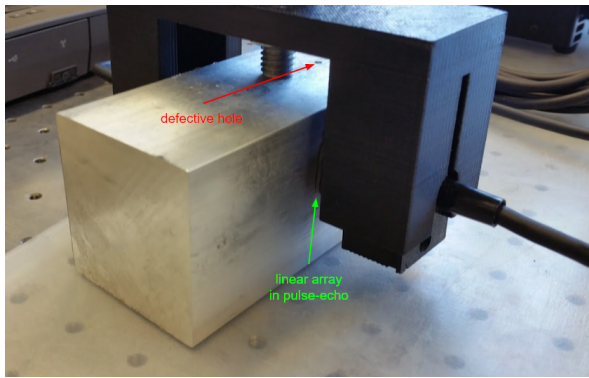


Figure 7. Image of the linear array on the side of the aluminum block.

#### 5.4. Waveform comparison

The simulation provided a FMC, consisting of all the waveforms for each transmitter's excitation. To validate the results of the simulation, waveforms were also experimentally gathered later from an aluminum block of the same dimensions and defect size. Some waveform results are shown below.

These waveforms are very similar and therefore, validate the simulation model.

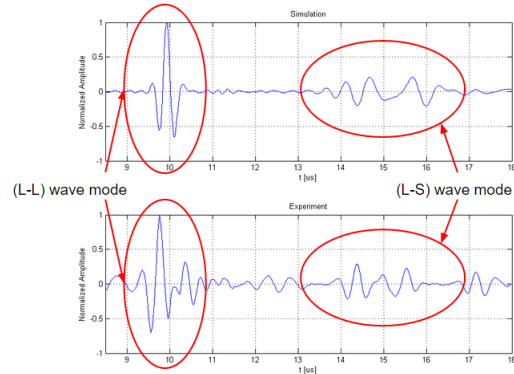


Figure 8. Waveforms extracted for element 28 firing an excitation and element 8 receiving. Top: Simulation results. Bottom: Experimental results.

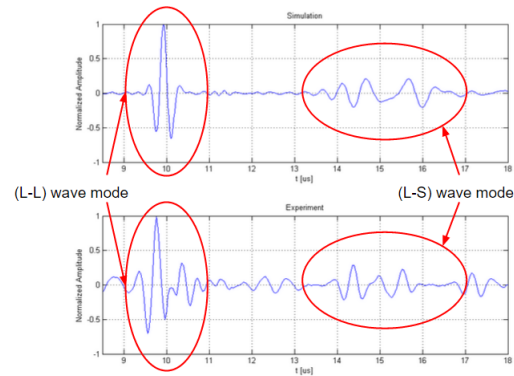


Figure 9. Waveforms extracted for element 12 firing an excitation and element 2 receiving. Top: Simulation results. Bottom: Experimental results.

### 5.5. Results

Images generated from the frameworks of: DAS, DAS with GMC, MVD, and MVD with GMC are produced from the simulated waveforms. The images are shown below. The last set of images, are an incoherent sum of the ( $L - L$ ) and ( $L - S$ ) wave mode images.

#### 5.5.1. Simulation results

For a simulated defect at (28mm, 30mm), the simulations prove to be effective. In figures 10, 11, 13, 14, and 16, the images produced with the addition of the GMC show significant improvement. Furthermore, in figures 12 and 15, the resolution in both axial and lateral directions have a higher dynamic range when the images are produced with the GMC.

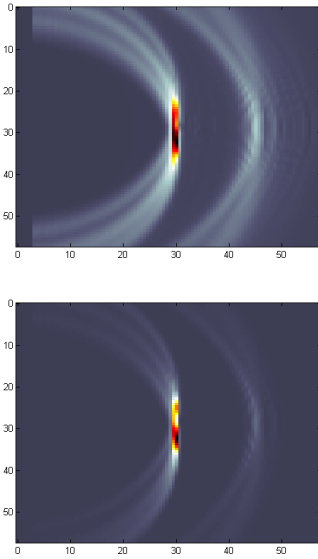


Figure 10. Simulation: Images for conventional DAS (first), DAS with GMC (second) using the  $(L - L)$  wavemode combination from simulation. (Dimensions are in [mm].)

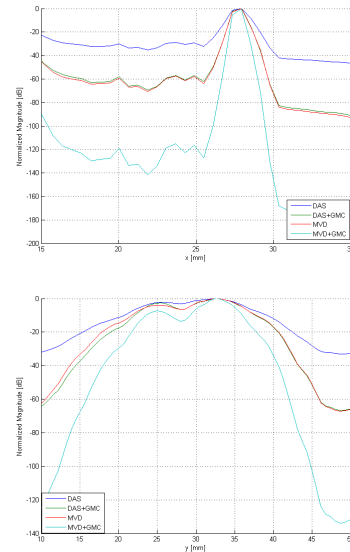


Figure 12. Simulation: (L-L) Point spread function for the four methods mentioned in Figures 10 and 11. Top: Lateral resolution. Bottom: Axial resolution.

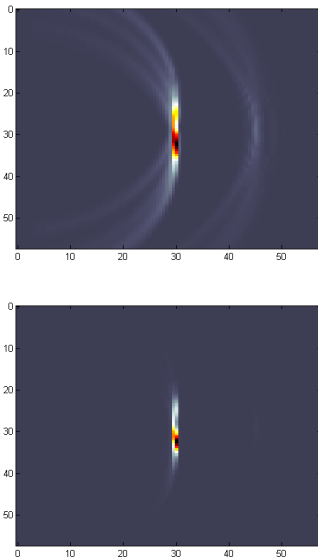


Figure 11. Simulation: Images for conventional MVD (first), MVD with GMC (second) using the  $(L - L)$  wavemode combination from simulation. (Dimensions are in [mm].)

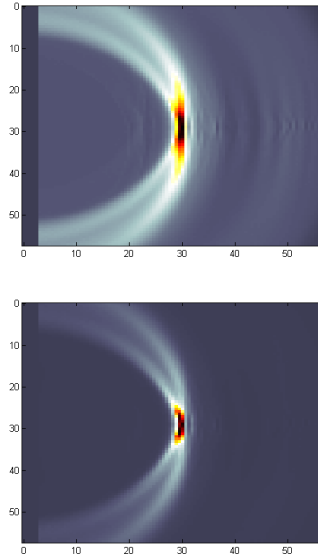


Figure 13. Simulation: Images for conventional DAS (first), DAS with GMC (second) using the  $(L - S)$  wavemode combination from simulation. (Dimensions are in [mm].)

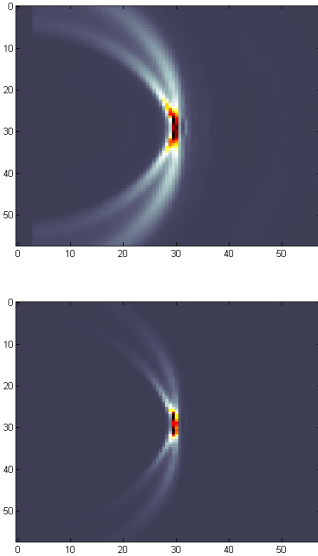


Figure 14. Simulation: Images for conventional MVD (first), MVD with GMC (second) using the  $(L-S)$  wavemode combination from simulation. (Dimensions are in [mm].)

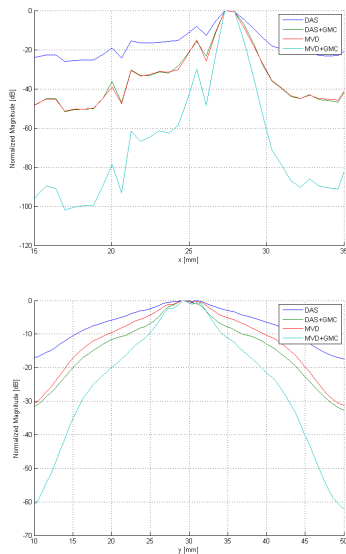


Figure 15. Simulation:  $(L-S)$  Point spread function for the four methods mentioned in Figures 13 and 14. Top: Lateral resolution. Bottom: Axial resolution. (Dimensions are in [mm].)

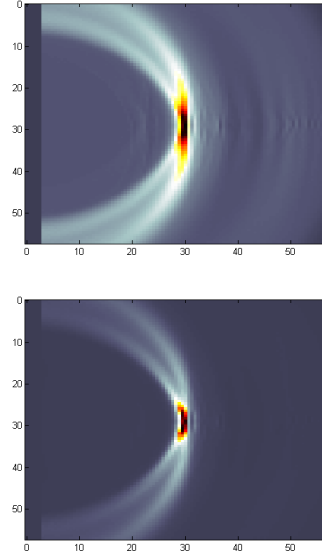


Figure 16. Simulation: Images for conventional DAS (first), DAS with GMC (second) using both the  $(L-L)$  and  $(L-S)$  wavemode combination from simulation. (Dimensions are in [mm].)

### 5.5.2. Experimental results

For a drilled hole at about  $(29mm, 29mm)$ , the images prove to be very clear. In figures 17, 18, 20, 21, and 23, the images produced with the addition of the GMC show significant improvement. Furthermore, in figures 19 and 22, the resolution in both axial and lateral directions have a higher dynamic range when the images are produced with the GMC. The experimental results are very comparable to the simulation results.

## 6. CONCLUSION

Over all, with the addition of the global matched coefficients, the images have higher dynamic resolution in both lateral and axial directions. Accuracies are similar for all beamforming frameworks, however, the SNR improves with the addition of GMC. For all cases, the lateral resolution is superb. In the  $(L-S)$  modes, the resolution is limited to identifying scatterers that are at least  $6mm$  apart. Case 2 study shows this. However, it is effective in identifying the existence of a scatterer at that location. The images from the  $(L-L)$  wave mode are excellent, and show very clear promise in the ability to characterize and image defects.

From this, the imaging frameworks benefit from the addition of GMC, and with defects less than  $6mm$  apart, only the  $(L-L)$  mode is effective in distinguishing the defects from one another.

A new adaptive beamforming framework with the GMC was presented and formulated using a unique set of replica vec-

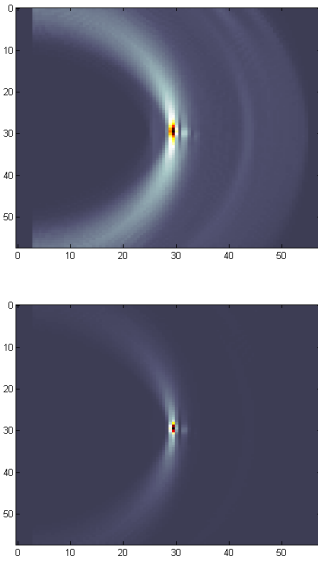


Figure 17. Experimental: Images for conventional DAS (first), DAS with GMC (second) using the  $(L - L)$  wave-mode combination from experimental data. (Dimensions are in [mm].)

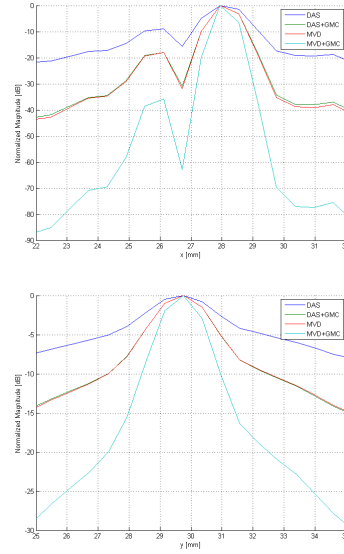


Figure 19. Experimental: With (L-L) wave mode: Point spread function for the four methods mentioned in Figures 10 and 11. Top: Lateral resolution. Bottom: Axial resolution. (Dimensions are in [mm].)

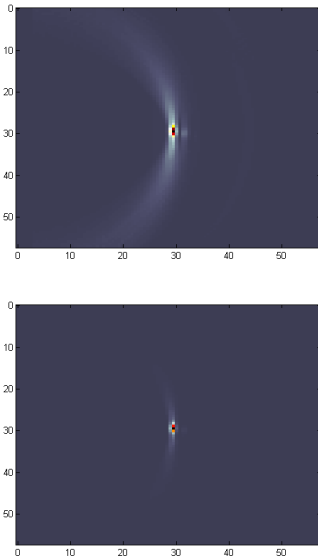


Figure 18. Experimental: Images for conventional MVD (first), MVD with GMC (second) using the  $(L - L)$  wave-mode combination from experimental data. (Dimensions are in [mm].)

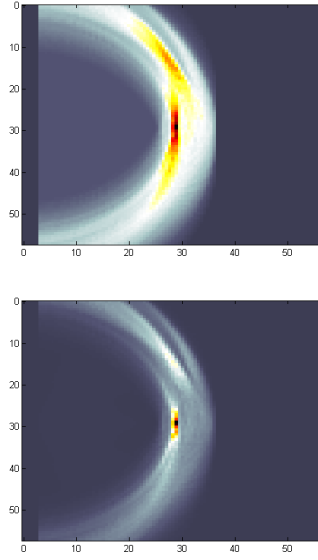


Figure 20. Experimental: Images for conventional DAS (first), DAS with GMC (second) using the  $(L - S)$  wave-mode combination from experimental data. (Dimensions are in [mm].)

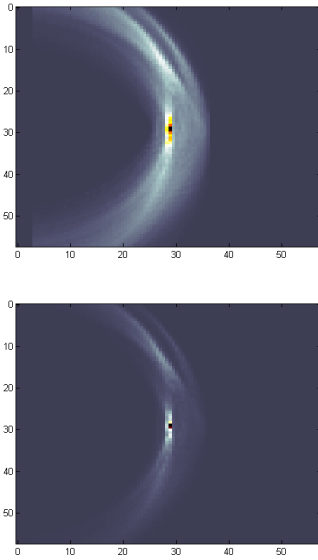


Figure 21. Experimental: Images for conventional MVD (first), MVD with GMC (second) using the  $(L - S)$  wave mode combination from experimental data. (Dimensions are in [mm].)

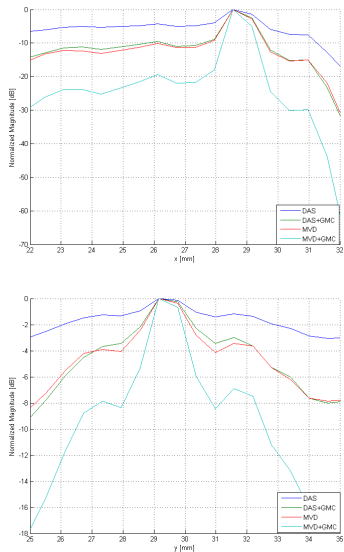


Figure 22. Experimental: With  $(L-S)$  wave mode: Point spread function for the four methods mentioned in Figures 20 and 21. Top: Lateral resolution. Bottom: Axial resolution. (Dimensions are in [mm].)

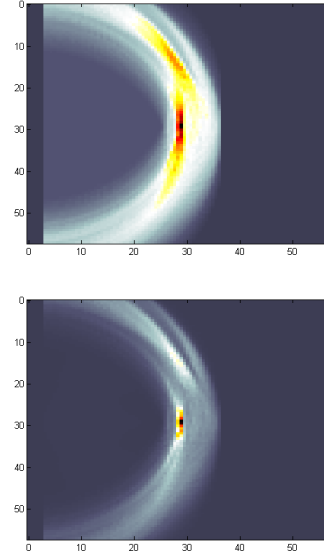


Figure 23. Experimental: Images for conventional DAS (first), DAS with GMC (second) using both the  $(L - L)$  and  $(L - S)$  wave mode combination from experimental data. (Dimensions are in [mm].)

tors. These vectors are modeled from specific wavemodes, specifically the longitudinal and shear in transmission, and the longitudinal wavemode in reception. These replica vectors exploit the out-of-plane particle displacement field with respect to the transducers, effectively modeling the expected relative amplitudes of the received signals.

The GMC framework was applied to the conventional DAS and MVD frameworks. The reconstruction of images using ultrasound are presented in both of DAS and MVD frameworks of a defected aluminum block. Additionally, images constructed utilizing the GMC weights are also presented.

The figures show a substantial improvement in the clarity and precision of the defect in the steel. When comparing the point spread functions, the GMC weights using the adaptive wavemode-based replica vectors result in the higher ratio of defect scattering to noise scattering and minimize artificial scatterings.

This paper introduced new adaptive weights based on replica vectors modeled from the displacement structure of specific propagating wavemodes. The new approach shows excellent results in a simulation of an aluminum block with an artificial hole defect and experimental results validate these simulations. Further studies will exploit other expected response features to be used in the GMC formulations.

**REFERENCES**

*Advanced oem systems.* (n.d.). <http://aos-ndt.com/>.

- Austeng, A., Nilsen, C., Jensen, A., Nasholm, S., & Holm, S. (2011, Oct). Coherent plane-wave compounding and minimum variance beamforming. In *Ultrasonics symposium (ius), 2011 ieee international* (p. 2448-2451).
- Baggeroer, A., Kuperman, W., & Mikhalevsky, P. (1993, Oct). An overview of matched field methods in ocean acoustics. *Oceanic Engineering, IEEE Journal of*, 18(4), 401-424.
- Chen, X., Michaels, J. E., & Michaels, T. E. (2014, Oct). Load-enhanced lamb wave techniques for characterization of scatterers in structures with complex geometries. *Materials Evaluation*, 72, 1314-1324.
- Corciulo, M., Roux, P., Campillo, M., Dubucq, D., & Kuperman, W. (2012). Multiscale matched-field processing for noise-source localization in exploration geophysics. *Geophysics*, 77(5), KS33-KS41.
- Ekroll, I., Swillens, A., Segers, P., Dahl, T., Torp, H., & Lovstakken, L. (2013, April). Simultaneous quantification of flow and tissue velocities based on multi-angle plane wave imaging. *Ultrasonics, Ferroelectrics, and Frequency Control, IEEE Transactions on*, 60(4), 727-738.
- Frazier, C., & O'Brien, W. (1998, Jan). Synthetic aperture techniques with a virtual source element. *Ultrasonics, Ferroelectrics, and Frequency Control, IEEE Transactions on*, 45(1), 196-207.
- Garcia, D., Tarnec, L., Muth, S., Montagnon, E., Poree, J., & Cloutier, G. (2013, Sep). Stolt's f-k migration for plane wave ultrasound imaging. *Ultrasonics, Ferroelectrics, and Frequency Control, IEEE Transactions on*, 60(9), 1853-1867.
- Hall, J., & Michaels, J. (2010, October). Minimum variance ultrasonic imaging applied to an in situ sparse guided wave array. *Ultrasonics, Ferroelectrics, and Frequency Control, IEEE Transactions on*, 57(10), 2311-2323.
- Kuperman, W., & Turek, G. (1997). Matched field acoustics. *Mechanical systems and signal processing*, 11(1), 141-148.
- Lockwood, G., Talman, J., & Brunke, S. (1998, July). Real-time 3-d ultrasound imaging using sparse synthetic aperture beamforming. *Ultrasonics, Ferroelectrics, and Frequency Control, IEEE Transactions on*, 45(4), 980-988.
- MATLAB. (2010). *version 7.10.0 (r2010a)*. Natick, Massachusetts: The MathWorks Inc.
- Nikolov, S., & Jensen, J. (2000, Oct). 3d synthetic aperture imaging using a virtual source element in the elevation plane. In *Ultrasonics symposium, 2000 ieee* (Vol. 2, p. 1743-1747 vol.2).
- Salles, S., Liebgott, H., Basset, O., Cachard, C., Vray, D., & Lavarello, R. (2014, November). Experimental evaluation of spectral-based quantitative ultrasound imaging using plane wave compounding. *Ultrasonics, Ferroelectrics, and Frequency Control, IEEE Transactions on*.
- Treeby, B., Jaros, J., Rohrbach, D., & Cox, B. (2014, Sept). Modelling elastic wave propagation using the k-wave matlab toolbox. In *Ultrasonics symposium (ius), 2014 ieee international* (p. 146-149).

## BIOGRAPHIES

**Thompson Vu Nguyen** was born in Fountain Valley, California in 1989. He is a graduate student researcher pursuing his Ph.D. at the Structural Engineering Department at the University of California, San Diego. Also at the University of California, San Diego is where he obtained his M.S. in Structural Engineering (2013), his B.A. in Mathematics (2011) and B.S. in Structural Engineering (2011).